the deviated jet. Physically, it is linked to the unsteady entrainment on the uncontrolled side.

C. Discussion on the Control Mechanism

The phase-averaged measurements bring some physical insight into the control mechanism. Control pulsing affects the flow near the diffuser wall by means of a periodic train of eddies. On one side of these eddies, their flux is part of the jet flow, and on the other side they roll on the diffuser wall with a slight sliding, which is indicated by the reverse flow along the wall. Thus, the presence of a diffuser at the jet mouth would permit the use of the main flow energy to deviate the jet by the Coanda effect. The Coanda effect acts on the periodic train of vortical structures generated by the control, which are attached to the main flow. These structures permit the jet to come closer to the diffuser wall. The present experiment is almost a limiting case where one and only one control structure is always inside the diffuser: the ratio of the control wavelength to the diffuser wall length is about one.

The importance of the suction phase in the control process can also be discussed. As in Smith and Gleser's work,[8] the synthetic jet injector used in the present investigation was not symmetrical, with a slight streamwise extension on one side, so that the suction of the main jet fluid is favored. This direct suction of the jet flow, which appeared to be very efficient in deviating laminar jets,[8] would also have some effect on the turbulent jet being studied. The diffuser wall would then take advantage of this early deviation for the subsequent eddy dynamics.

IV. Conclusions

This experimental investigation has shown the efficiency of a wall pulsing control applied on a plane turbulent jet with a short wide-angle diffuser attached to the jet exit. The wall pulsing increases the jet lateral expansion. Pulsing on both sides of the jet was also found to be the most efficient for lateral expansion: spreading parameter of the order of 2×0.25 have been obtained compared to 0.30 for one-side control and 2×0.10 without control. The inner structure of the jet was found to be strongly modified, with a shortening of the potential core and with the generation of highly periodic large-scale structures. The mechanism of the control was also investigated. The control system generated vortex structures, which stuck to the diffuser wall by the Coanda effect and then enlarged the jet. Concerning the control frequency, it is also interesting to note that it was relatively low, hence permitting extensions towards higher Reynolds numbers and specially higher jet velocities.

References

[1]Smith, D., Amitay, M., Kibens, V., Parekh, D., and Glezer, A., "Modification of Lifting Body Aerodynamics Using Synthetic Jet Actuators," AIAA Paper 98-0209, Jan. 1998.

[2]Béra, J. C., Michard, M., Sunyach, M., and Comte-Bellot, G., "Changing Lift and Drag by Jet Oscillation: Experiments on a Circular Cylinder with Turbulent Separation," *European Journal of Mechanics B—Fluids*, Vol. 19, 2000, pp. 575–595.

[3]Seifert, A., Bachar, T., Koss, D., Shepsheplovich, M., and Wygnanski, I., "Oscillatory Blowing: Tool to Delay Boundary-Layer Separation," *AIAA Journal*, Vol. 31, No. 11, 1993, pp. 2052–2060.

[4]MacManus, K., and Magill, J., "Airfoil Performance Enhancement Using Pulsed Jet Separation Control," AIAA Paper 97-1971, July 1997.

[5]Kwong, A. H. M., and Dowling, A. P., "Active Boundary-Layer Control in Diffuser," *AIAA Journal*, Vol. 32, 1994, pp. 2409–2414.

[6]Ben Chiekh, M., Béra, J. C., Michard, M., and Sunyach, M., "Contrôle par Jet Pulsé de l'Écoulement Dans un Divergent Court à Grand Angle (Pulsed Jet Control of a Short Diffuser)," *Compte Rendu de l'Académie des Sciences de Paris*, Vol. 328, Série II.b, pp. 749–756.

[7]Smith, B. L., and Glezer, A., "Vectoring and Small-Scale Motions Effected in Free Shear Flows Using Synthetic Jet Acuators," AIAA Paper 97-0213, Jan. 1997.

[8]Smith, B. L., and Glezer, A., "Jet Vectoring Using Synthetic Jets," *Journal of Fluid Mechanics*, Vol. 458, 2002, pp. 1–34.

[9]Pack, L. G., and Seifert, A., "Periodic Excitation for Jet Vectoring and Enhanced Spreading," AIAA Paper 99-0672, Jan. 1999.

[10]Parekh, D. E., Kibens, V., Glezer, A., Wiltse, J. M., and Smith, D. M., "Innovative Jet Control: Mixing Enhancement Experiments," AIAA Paper 96-0308, Jan. 1996.

[11]Freund, J. B., and Moin, P., "Jet Mixing Enhancement by High-Amplitude Fluidic Actuation," *AIAA Journal*, Vol. 38, No. 10, 2000, pp. 1863–1870.

[12]Béra, J. C., Michard, M., Grosjean, N., and Comte-Bellot, G., "Flow Analysis of 2D Pulsed Jets by Particle Image Velocimetry," *Experiments in Fluid*, Vol. 30, No. 5, 2001, pp. 519–532.

[13]Raffel, M., Willert, C. E., and Kompenhans, J., *Particle Image Velocimetry—A Practical Guide*, Springer-Verlag, Berlin, 1998, pp. 134–146.

[14]Michard, M., Graftieaux, L., Lollini, L., and Grosjean, N., "Identification of Vortical Structures by a Non Local Criterion: Application to PIV Measurement and DNS-LES Results of Turbulent Rotating Flows," 11th Symposium on Turbulent Shear Flows, Session 28, Institut National Polytechnique de Grenoble/CNRS/Université Joseph Fourier, Sept. 1997, pp. 25–30.

[15]Kotsovinos, N. E., "A Note on the Spreading Rate and Virtual Origin of a Plane Turbulent Jet," *Journal of Fluid Mechanics*, Vol. 77, Pt. 2, 1976, pp. 305–311.

A. Plotkin
Associate Editor

Local Coordinate Approach in Meshless Local Petrov–Galerkin Method for Beam Problems

I. S. Raju*
NASA Langley Research Center, Hampton, Virginia 23681-2199
and
D. R. Phillips†
Joint Institute for Advancement of Flight Sciences—George Washington University, Hampton, Virginia 26381-2199

Introduction

MESHLESS methods are increasingly being viewed as an alternative to the finite element method.[1–5] Recently, a meshless local Petrov–Galerkin (MLPG) method has been presented for C^0 and C^1 problems.[4–6] In these methods, moving least-squares (MLS) interpolants[1] are used for C^0 problems, and generalized MLS interpolants are used for C^1 problems.[5] References 2–6 showed excellent performance of the MLPG method for potential and elasticity problems and a good performance for beam problems.

When all of the chosen parameters in the MLPG method are held constant and the number of nodes in the models is consistently increased, the error norms do not decrease; rather they show increases compared to coarser idealizations. The reasons for this behavior are studied. A local coordinate approach to the MLS interpolation is proposed. The proposed local coordinate approach is implemented and evaluated by applying it to three simple test cases.

Behavior of the MLPG Method with Mesh Refinement

The notation of Ref. 5 is used in this Note for brevity and convenience in presentation. The MLPG equations are

$$\boldsymbol{K}_i^{(\text{node})}\boldsymbol{d} + \boldsymbol{K}_i^{(\text{bdy})}\boldsymbol{d} - \boldsymbol{f}_i^{(\text{node})} - \boldsymbol{f}_i^{(\text{bdy})} = \boldsymbol{0} \tag{1}$$

Received 15 March 2002; revision received 21 November 2002; accepted for publication 5 January 2003.

*Senior Technologist, Structures and Materials Competency, Mail Stop 240. Fellow AIAA.

†Graduate Student; currently Aerospace Engineer, Lockheed Martin Space Operations, Mail Stop 240, Hampton, VA 23681-2199.

Table 1 Exponents of error norm $\|E\|_1$ of the residuals for six models and for two basis functions for both the global and local coordinate approach ($m = 3$ quadratic basis, $m = 4$ cubic basis)

	Global method						Local method					
	$u = c_0$		$u = c_1 x$		$u = c_2 x^2$		$u = c_0$		$u = c_1 x$		$u = c_2 x^2$	
Nodes in model	$m = 3$	$m = 4$	$m = 3$	$m = 4$	$m = 3$	$m = 4$	$m = 3$	$m = 4$	$m = 3$	$m = 4$	$m = 3$	$m = 4$
5[a]	−14	−12	−14	−13	−14	−13	−14	−13	−15	−14	−14	−13
9[a]	−13	−11	−13	−12	−13	−12	−13	−13	−14	−13	−13	−13
17[a]	−10	−10	−10	−10	−10	−10	−12	−12	−13	−12	−12	−12
33	−9	−5	−9	−6	−10	−6	−12	−11	−12	−12	−12	−11
65	−6	−2	−7	−3	−6	−2	−11	−11	−11	−11	−11	−11
129	−4	+0	−5	+0	−4	+0	−10	−10	−10	−11	−10	−10

[a] $R_i/l = 3.5$.

where

$$\{\boldsymbol{d}\} = \{\hat{u}_1, \hat{\theta}_1, \hat{u}_2, \hat{\theta}_2, \ldots\}^T \tag{2}$$

are the fictitious nodal values of deflections u and slopes θ, and the matrices in Eq. (1) are defined as in Eqs. (35) and (36g) of Ref. 5.

The MLPG equations are derived using a weighted residual weak form of the governing equations. The trial functions used for the beam problems are derived using the generalized MLS interpolation[5] as

$$u(x) = \sum_{i=1}^{n} \hat{u}_i \psi_i^{(u)}(x) + \hat{\theta}_i \psi_i^{(\theta)}(x) \tag{3}$$

where

$$\psi_i^{(u)}(x) = \sum_{j=1}^{m} p_j(x)[\boldsymbol{A}^{-1}\boldsymbol{P}^T\boldsymbol{w}]_{ji}$$

$$\psi_i^{(\theta)}(x) = \sum_{j=1}^{m} p_j(x)[\boldsymbol{A}^{-1}\boldsymbol{P}_x^T\boldsymbol{w}]_{ji} \tag{4}$$

with

$$[\boldsymbol{A}] = \boldsymbol{P}^T\boldsymbol{w}\boldsymbol{P} + \boldsymbol{P}_x^T\boldsymbol{w}\boldsymbol{P}_x \tag{5}$$

In Eq. (5), $\boldsymbol{P}$ is an (n, m) matrix, and $\boldsymbol{w}$ is an (n, n) matrix defined as

$$[\boldsymbol{P}] = [\boldsymbol{p}(x_1) \quad \boldsymbol{p}(x_2) \quad \ldots \quad \boldsymbol{p}(x_n)]^T \tag{6}$$

$$\boldsymbol{w} = \begin{bmatrix} w_1(\bar{x}) & & & \\ & w_2(\bar{x}) & & \\ & & \ddots & \\ & & & w_n(\bar{x}) \end{bmatrix} \tag{7}$$

where $\bar{x} = x - x_i$ and

$$\boldsymbol{p}^T(x) = \lfloor 1, x, x^2, \ldots x^{m-1} \rfloor$$

$$\boldsymbol{p}_x^T(x) = \frac{\mathrm{d}\boldsymbol{p}^T}{\mathrm{d}x} = [0, 1, 2x, \ldots (m-1)x^{m-2}] \tag{8}$$

with $(m-1)$ as the order of the basis function $\boldsymbol{p}(x)$ used in the MLS approximation. The weight functions $w_i(\bar{x})$ chosen are

$$w_i(\bar{x}) = \left[1 - (d_i/R_i)^2\right]^4 \quad \text{if} \quad d_i \le R_i, \quad = 0 \quad \text{if} \quad d_i > R_i \tag{9a}$$

$$w_i(\bar{x}) = \begin{cases} 1 - 6(d_i/R_i)^2 + 8(d_i/R_i)^3 - 3(d_i/R_i)^4 & \text{if} \quad 0 \le d_i \le R_i \\ 0 & \text{if} \quad d_i \ge R_i \end{cases} \tag{9b}$$

where $d_i = \|x - x_i\|$. The test function $v_i(x)$ in the MLPG weak form is chosen as

$$v_i(x) = \left[1 - (d_i/R_o)^2\right]^4 \quad \text{if} \quad d_i \le R_o, \quad = 0 \quad \text{if} \quad d_i > R_o \tag{10}$$

Note that the lengths R_i and R_o in Eqs. (9) and (10) are user defined in the MLPG method.

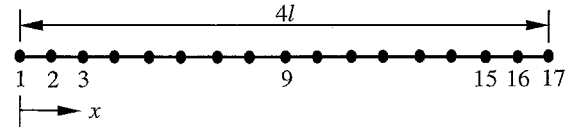

Fig. 1 Beam and a 17-node model.

In the current implementation, a beam of length $4l$ is considered as the choice of unit beam length l would mask numerical errors. Six models with 5, 9, 17, 33, 65, and 129 nodes uniformly distributed along the length of the beam are considered. The model with 17 nodes is presented in Fig. 1. The distances between the nodes (Δ/l) in these models are 1.0, 0.5, 0.25, 0.125, 0.0625, and 0.03125 for the 5-, 9-, 17-, 33-, 65-, and 129-node models, respectively. The (R_o/l) in the test functions [Eq. (10)] in each of these six models is different and is chosen equal to (2Δ). The (R_i/l) in Eq. (9) is chosen to be $(R_i/l = 3.5)$ for the 5-, 9-, and 17-node models and $(R_i/l = 16\Delta)$ for the 33-, 65-, and 129-node models. Two types of basis functions, quadratic basis $(1, x, x^2)$ and cubic basis $(1, x, x^2, x^3)$, are used. System matrices in Eq. (1) are developed with these parameters. To evaluate the system matrices developed for the six models, two rigid-body conditions and a constant-curvature condition were considered. These can be written as follows.

Rigid-body translation:

$$u(x) = c_0, \qquad \theta = \frac{\mathrm{d}u}{\mathrm{d}x} = 0 \tag{11a}$$

Rigid-body rotation:

$$u(x) = c_1 x, \qquad \theta = c_1 \tag{11b}$$

Constant curvature:

$$u(x) = c_2 x^2, \qquad \theta = 2c_2 x \tag{11c}$$

where c_0, c_1, and c_2 are arbitrary constants. The third condition in Eq. (11) corresponds to the problem of a cantilever beam with a moment, $M = EI \cdot (\mathrm{d}^2u/\mathrm{d}x^2) = 2EIc_2$, applied at $x = 4l$. The problems described by Eq. (11) are simple test problems and should be reproduced exactly by the MLPG method when quadratic or higher bases are used.

The $\{\boldsymbol{d}\}$ vectors that correspond to each of the conditions in Eq. (11) (and in the absence of any other loading) when used in Eq. (1) should result in a null right-hand vector if the $\boldsymbol{K}_i^{(\mathrm{node})}$ is evaluated exactly. In general, the product results in a residual $\{\boldsymbol{r}\}$ vector as

$$\boldsymbol{K}_i^{(\mathrm{node})}\{\boldsymbol{d}\} = \{\boldsymbol{r}\} \tag{12}$$

Each of the components of the vector $\{\boldsymbol{r}\}$ is nearly equal to machine zero if $\boldsymbol{K}_i^{(\mathrm{node})}$ is evaluated accurately. To quantify the residual, an error norm of $\{\boldsymbol{r}\}$ is computed as

$$\|E\|_1 = \sqrt{\frac{1}{N_d}\sum_{k=1}^{N_d} r_k^2} \tag{13}$$

where r_k is the kth component of the vector $\{\boldsymbol{r}\}$ in Eq. (12) and N_d is the degrees of freedom in the model. Table 1 presents the exponents

Table 2 Comparison of the condition numbers of the [A] matrices at various locations on the beam using global and local coordinate methods

	Number of nodes in the model					
Location on the beam ($x/4l$)	5[a]	9[a]	17[a]	33	65	129
			Global method conditioning number			
0.0	0.631e+3	0.106e+4	0.930e+3	0.271e+3	0.267e+3	0.189e+4
0.5	0.231e+5	0.268e+5	0.272e+5	0.785e+5	0.904e+6	0.131e+8
1.0	0.914e+6	0.771e+6	0.127e+7	0.422e+8	0.153e+10	0.365e+11
			Local method conditioning number			
0.0	0.634e+3	0.106e+4	0.930e+3	0.271e+3	0.267e+3	0.189e+4
0.5	0.478e+3	0.496e+2	0.411e+2	0.111e+2	0.153e+2	0.141e+3
1.0	0.632e+3	0.106e+4	0.930e+3	0.271e+3	0.267e+3	0.189e+4

[a] $R_i/l = 3.5$.

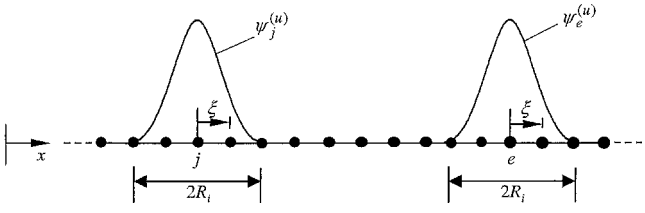

Fig. 2 Local coordinate definitions.

of the error norm $\|E\|_1$ (for example, -14 in Table 1 represents a norm of the order 1×10^{-14}) for the three conditions in Eq. (11) when the weight function in Eq. (9b) is used. As seen from Table 1, the $\|E\|_1$ deteriorates with model refinement and for higher-order basis. Closer examination of the residuals for each of the six models showed that the residuals were of machine accuracy for nodes near the origin, whereas the residuals were largest at nodes farthest from the origin. This observation was confirmed by running different cases with the origin at different locations along the length of the beam. Also, the residuals were largest for the models with the largest number of nodes.

Closer scrutiny of the computations showed that the numerical values of the shape functions for nodes that are systematically located about the center of the beam (for example, nodes 3 and 15, 2 and 16, and 1 and 17 in the 17-node model of Fig. 1) are not exactly identical as expected. These differences increased with model refinement and when a higher basis was used. The error norm in Table 1 can be improved by using higher precision computations or inversion routines. However, a much simpler alternative to improve the accuracy is presented next.

Local Coordinate Approach

In the MLS interpolation, the basis functions are in terms of the global coordinate x. The $[\boldsymbol{A}]$ matrix thus formed using this basis is generally of the form [see Eq. (16), Ref. 5]

$$[\boldsymbol{A}] = \sum_{k=1}^{M} \left\{ w_k(\bar{x})\boldsymbol{p} \cdot \boldsymbol{p}^T + w_k(\bar{x})\boldsymbol{p}_x \cdot p_x^T \right\} \tag{14}$$

where $\bar{x} = x - x_j$ and M are the number of nodes in the domain of definition of node j for which the $[\boldsymbol{A}]$ matrix is being computed. (For convenience in presentation, the $[\boldsymbol{A}]$ matrices thus formed will be referred to as the global method.) As the order of the polynomial basis increases, the conditioning of the $[\boldsymbol{A}]$ matrix deteriorates. For example, the matrix $[\boldsymbol{A}]$ will have terms like 1, x^2, x^4, x^6 on the diagonal for a cubic basis function. The $[\boldsymbol{A}]$ matrices for nodes near the origin and the $[\boldsymbol{A}]$ matrices for nodes farthest from the origin will be different. The conditioning is worse for $[\boldsymbol{A}]$ matrices for nodes farthest from the origin. This explains the differences in the error norms observed in Table 1. The situation can be easily rectified if the MLS approximation is defined not in terms of a global basis, but rather in terms of a local basis. Figure 2 shows two identical shape functions, one centered at node j, and the other centered at node e.

The global approximation for

$$\begin{aligned} u(x) &= \boldsymbol{p}^T(\boldsymbol{x})\boldsymbol{a}(\boldsymbol{x}) \\ &= a_1 + a_2 x + a_3 x^2 + \cdots + a_m x^{m-1} \end{aligned} \tag{15}$$

can be rewritten in the neighborhood of node j, recognizing that $x = x_j + \xi$, where ξ is a local coordinate measured from node j, as

$$\begin{aligned} u(x) &= a_1 + a_2(x_j + \xi) + a_3(x_j + \xi)^2 + \cdots \\ &= \left(a_1 + a_2 x_j + a_3 x_j^2\right) + (a_2 + 2a_3 x_j + \cdots)\xi + (a_3 + \cdots)\xi^2 \\ &= b_1 + b_2\xi + b_3\xi^2 + \ldots \end{aligned} \tag{16}$$

where $b_i, i = 1, \ldots, m-1$, are the new undetermined coefficients in the MLS approximation. (A similar local coordinate transformation can be affected for node e in Fig. 2 as $x = x_e + \xi$.) The $[\boldsymbol{A}]$ matrix then is computed in a similar manner as in Eq. (14) but with

$$\begin{aligned} \boldsymbol{p}^T(\xi) &= \lfloor 1, \xi, \xi^2, \ldots \xi^{m-1} \rfloor \\ \boldsymbol{p}_x^T(\xi) &= [0, 1, 2\xi, 3\xi^2, \ldots (m-1)\xi^{(m-2)}] \end{aligned} \tag{17}$$

as

$$\frac{\mathrm{d}}{\mathrm{d}x}(\,) = \frac{\mathrm{d}}{\mathrm{d}\xi}(\,)$$

Local Coordinate Approach Results

The local coordinate approach is implemented in the evaluation of the shape functions and their derivatives for all of the nodes in the six MLPG models of the beam. Table 2 compares the condition numbers of the $[\boldsymbol{A}]$ matrices at various locations on the beam using global and local coordinate methods. The condition numbers are evaluated using routines available in NAPACK and the procedure outlined in Refs. 7 and 8. When the global coordinate method is used, the condition numbers of the $[\boldsymbol{A}]$ matrices for nodes farthest from the origin are much larger (suggesting poor conditioning) than the nodes closest to the origin. The conditioning numbers of the $[\boldsymbol{A}]$ matrices vastly improve when the local coordinate method is used, clearly demonstrating the advantages of the local coordinate method. The error norms obtained using the local coordinate approach are included in the right-hand half of Table 1. As expected, all models and the quadratic and cubic basis functions produced the error norms close to machine accuracy, suggesting that the local coordinate approach produces accurate results compared to the global coordinate approach.

Computational Advantage of the Local Coordinate Approach

In the conventional MLPG implementation, the $[\boldsymbol{A}]$ matrix is calculated and inverted at every node in the model. When using the local coordinate methodology with uniform nodal spacing, the shape

functions are exactly identical for nodes whose R_i places the entire shape function in the interior of the domain of the problem. Hence, for those nodes the $[\boldsymbol{A}]$ matrices are identical. As such, considerable reduction in computational effort and cost can be achieved by the proposed local coordinate approach, thus eliminating a perceived disadvantage of the MLPG method.

Conclusions

The meshless local Petrov–Galerkin (MLPG) method for beam problems (C^1 problems) showed that the solutions deteriorated as the number of nodes in the models were progressively increased. Closer examination revealed that the moving least-squares (MLS) shape function calculations involved the computation of the $[\boldsymbol{A}]$ matrix and that this matrix became ill conditioned for nodes farthest from the origin. To overcome this difficulty, a local coordinate approach for the MLS basis functions was proposed. The proposed approach restored the accuracy of the MLPG method for beam problems.

Acknowledgment

The work of D. R. Phillips was funded by NASA Langley Research Center under Grant NCC1-384.

References

[1]Nayroles, B., Touzot, G., and Villon, P., "Generalizing the Finite Element Method: Diffuse Approximation and Diffuse Elements," *Computational Mechanics*, Vol. 10, 1992, pp. 307–318.

[2]Belytschko, T., Lu, Y. Y., and Gu, L., "Element-Free Galerkin Methods," *International Journal for Numerical Methods in Engineering*, Vol. 37, 1994, pp. 229–256.

[3]Krysl, P., and Belytschko, T., "Analysis of Thin Plates by the Element-Free Galerkin Method," *Computational Mechanics*, Vol. 17, 1995, pp. 26–35.

[4]Atluri, S. N., and Zhu, T., "A New Meshless Local Petrov–Galerkin (MLPG) Approach in Computational Mechanics," *Computational Mechanics*, Vol. 22, 1998, pp. 117–127.

[5]Atluri, S. N., Cho, J. Y., and Kim, H.-G., "Analysis of Thin Beams, Using the Meshless Local Petrov–Galerkin Method, with Generalized Moving Least Squares Interpolations," *Computational Mechanics*, Vol. 24, 1999, pp. 334–347.

[6]Phillips, D. R., and Raju, I. S., "Meshless Local Petrov–Galerkin Method for Bending Problems," NASA TM-2002-211936, Sept. 2002.

[7]Bathe, K.-J., *Finite Element Procedures*, 1st ed., Prentice–Hall, Upper Saddle River, NJ, 1996, p. 738.

[8]Chapra, S. C., and Canale, R. P., *Numerical Methods for Engineers*, 2nd ed., McGraw–Hill, New York, 1988, p. 257, URL: http://www.netlib.org/napack/.

S. Saigal
Associate Editor